Thermomechanics of candidate coatings for advanced gas reactor fuels

A. Nosek *, J. Conzen, H. Doescher, C. Martin, J. Blanchard

University of Wisconsin – Madison, 1500 Engineering Dr., Madison, WI 53706, United States

Abstract

Candidate fuel/coating combinations for an advanced, coated-fuel particle for a gas-cooled fast reactor (GFR) have been evaluated. These all-ceramic fuel forms consist of a fuel kernel made of UC or UN, surrounded with two shells (a buffer and a coating) made of TiC, SiC, ZrC, TiN, or ZrN. These carbides and nitrides are analyzed with finite element models to determine the stresses produced in the micro fuel particles from differential thermal expansion, fission gas release, swelling, and creep during particle fabrication and reactor operation. This study will help determine the feasibility of different fuel and coating combinations and identify the critical loads. The analysis shows that differential thermal expansion of the fuel and coating dictate the amount of stress for changing temperatures (such as during fabrication), and that the coating creep is able to mitigate an otherwise overwhelming amount of stress from fuel swelling. Because fracture is a likely mode of failure, a fracture mechanics study is also included to identify the relative likelihood of catastrophic fracture of the coating and resulting gas release. Overall, the analysis predicts that UN/ZrC is the best thermomechanical fuel/coating combination for mitigating the stress within the new fuel particle, but UN/TiN and UN/ZrN could also be strong candidates if their unknown creep rates are sufficiently large.
© 2007 Elsevier B.V. All rights reserved.

1. Introduction

One of the research needs for the gas-cooled fast reactor (GFR) is the development of a new fuel form. Most of the previous work in this area has focused on TRISO fuels, which may not be optimal for high temperature, high burn-up operation, so there is interest in an all-ceramic, bi-material fuel particle, which also can be considered an advanced BISO fuel particle. This type of fuel form has a fuel kernel and two ceramic outer layers. The central kernel consists of a spherical fuel particle surrounded by a ceramic coating which provides structural integrity and containment of fission products. In between the coating and the fuel, there is a buffer layer, which allows for changes in thermal expansion, swelling, and fission gas release pressure without creating an unacceptable amount of stress on the outer containment coating. The fuel particle layers are shown schematically in Fig. 1.

The buffer layer is porous in order to reduce its stiffness and the resulting pressure on the coating and to accommodate released fission gases. It is composed of the same material as the coating. By

---
* Corresponding author. Fax: +1 608 263 7451.
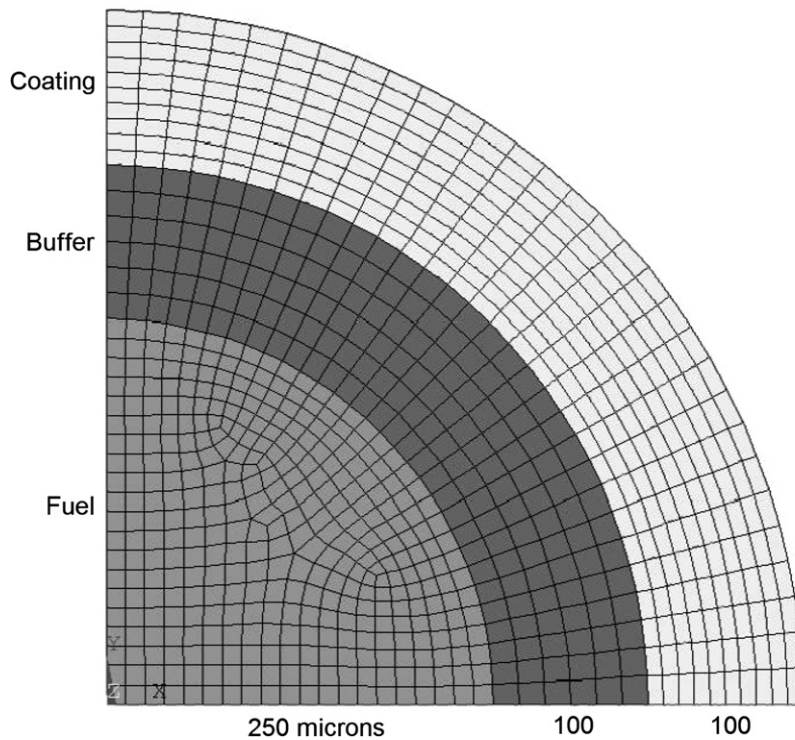 *E-mail address:* ajnosek@wisc.edu (A. Nosek).

Fig. 1. One quarter of the cross-section showing the layers of a BISO micro fuel particle.

using the same material for the buffer as the coating, there is reduced expansion mismatch and less chance of chemical incompatibilities. These advanced BISO fuel particles can be utilized by placing them in a ceramic matrix composed of the same material as the BISO fuel particles' outer ceramic coating. With this design, there is only one major interface of different materials: the fuel and the buffer.

The new BISO micro fuel particle materials must meet a variety of criteria. Coatings with significant neutron absorption cross-sections cannot be used, thus excluding many candidates. The potential coatings must have high melting points (in excess of 2000 °C), adequate thermal conductivity ($>$10 W/m-K) and toughness ($>$12 MPa-m$^{1/2}$), and acceptable response to high dose neutron damage [swelling $<$2% over service life ($\sim$80 dpa)]. Thus, the categories of materials with the highest potential for success for the GFR are carbide and nitride based ceramics [1].

In this paper, we predict the performance of these fuel particles from a thermomechanical perspective. The particles are modeled from fabrication, through startup and operation, and ultimately to shutdown. The analysis considers thermal expansion, swelling, creep, and internal pressure from gas release to predict the resulting stresses and to compare the relative performance of the candidate fuel and coating materials. The effect of the matrix, which will serve to reduce the fuel and coating stresses in this particle during reactor operation, is not considered here. Future work will include these effects.

2. Thermostructural modeling

The investigated material candidates for this study are SiC, TiC, ZrC, TiN, and ZrN for the ceramic coatings and buffer layers (with two different buffer densities), and UC and UN for the ceramic fuels. The baseline fuel form features a spherical fuel particle with a 250 μm radius and buffer and coating thicknesses of 100 μm. Since the analyzed buffer is to be of the same ceramic material as the coating, the two different buffer densities which were analyzed can be expressed as functions of porosity (75% and 50%).

Temperatures, stresses, and strains are calculated using ANSYS, a commercial finite element program. The models are built in 2-dimensional, axisymmetric geometry, permitting the consideration

of a spherical particle fuel form with a relatively small number of elements. The results here are all 1-dimensional, but the 2-dimensional model will be employed in future work, which will consider the effect of asymmetries in the fuel and coating. Inelastic behavior (swelling and creep) is included, as described later in this paper.

The analysis of the micro particle starts from its fabrication at 1600 °C. There are no stresses on the particle at this initial temperature and time. Depending on the fuel particle fabrication process, this may not always be true; however, it is assumed that these stresses would be insignificant compared to the stresses throughout the rest of its lifetime. The particle is allowed to cool to room temperature (20 °C), which is considered the 1st stress period to be analyzed. The particle is then heated to the temperature of reactor operation (1100 °C), and the micro particle is again analyzed at this 2nd period. In the 3rd stress period, the micro particle is analyzed continuously at this temperature for 3 years, while being subjected to the conditions of reactor operation. Lastly, the micro fuel particle is brought back down to room temperature and analyzed in the 4th stress period.

In all but the 3rd stress period (during reactor operation), where the micro fuel particle stays at a constant temperature of 1100 °C, the different thermal expansions of the layers of the micro fuel particle have the most significant effect on the stress in the coating. The stress from the thermal expansion in the fuel form occurs from the fuel shrinking more than the coating (and buffer) as the micro fuel particle cools. The coefficient of thermal expansion (CTE) dictates the amount of growth or shrinkage in the layers of the micro fuel particle due to changing temperatures. The CTE for the fuels and the coatings are shown in Fig. 2.

The larger the difference in CTE between the fuel and the coating, the larger the magnitude of the stress will be in the particle, because the difference in the rate at which the fuel and coating will shrink will be greater. From this, it is expected that UN and TiN have the most compatible thermal expansion of all the fuel and coating combinations.

Pressure from fission gas release of 4.84 MPa and fuel swelling rates of 9% per year for UC and 4.5% for UN are applied (Table 1), and thermal creep in the coatings is included (Table 2). No creep is expected in the fuel for this geometry, since the fuel is under a hydrostatic stress state. Coating (and buffer) swelling is assumed to be small compared to the fuel swelling, however Zinkle [5] reports this may not be the case at least for SiC. Irradiation creep in the coating could not be included, because of the lack of data.
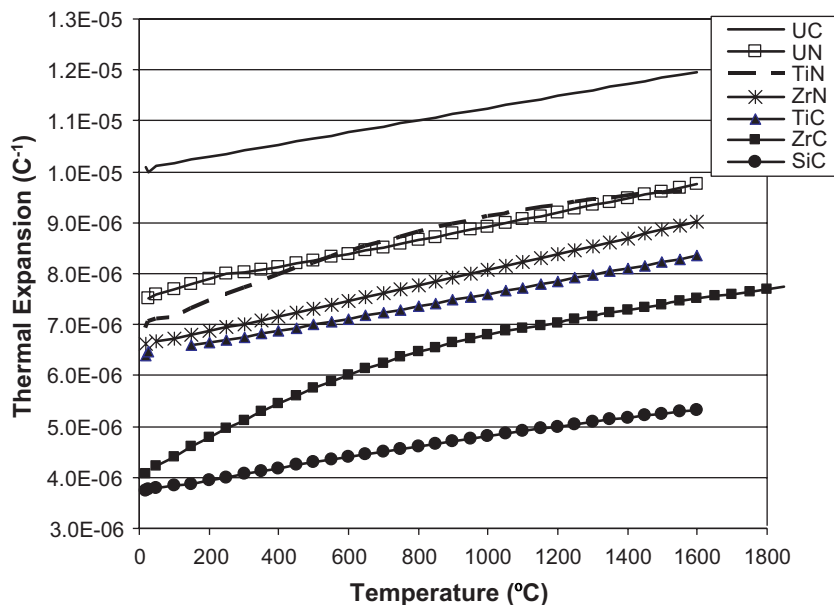

Fig. 2. Average coefficients of thermal expansion for different fuels (solid) and coatings (dashed) with all reference temperatures at 20 °C [2–4].

Table 1
Parameters used for baseline analyses

Assumptions		
Fuel fission rate density	3.00E + 13	fissions/cm^3-s
Fuel radius	250	μm
Buffer thickness	100	μm
Coating thickness	100	μm
Particle power	62.83	mW
Xe and Kr release fraction	0.95	%
gas pressure release	4.84	MPa/yr
Fuel density	0.0143	kg/cm^3
Annual burn-up	24551	MWD/MT-year
Annual swelling (UC, UN)	(9, 4.5)	%

Table 3
Elastic modulus for micro fuel particle materials at 20 °C

Material	Elastic modulus (Gpa)
UN	265
UC	225
TiC	470
SiC	410
ZrC	400
TiN	465
ZrN	380

One particular material property, the elastic modulus, has a strong effect on all the cases considered here. Under a given loading, such as differential expansions in the composite, the elastic modulus will determine the deformation required to maintain contact between the layers (assuming perfect adhesion). Materials with a high elastic modulus (which is characteristic of ceramics) will produce more stress for a given expansion. Table 3 is a comparison of all the room temperature elastic moduli for the different fuel and coating materials:

In a thermomechanical system such as a micro fuel particle, the choice of materials with lower elastic moduli like UC and ZrN will mitigate the stress. However, once a material is chosen the modulus can also be adjusted by altering the porosity of the coating. This is the main purpose of having a buffer layer, because the buffer's high porosity creates a low elastic modulus, accommodating deformation of the fuel without producing unnecessary stress or compromising the structural integrity of the coating. To approximate the elastic modulus of the buf-

fer as a function of porosity for a ceramic, the following relationship is employed [6]:

$$E_{\text{buffer}} \approx E_{\text{coating}}(1 - p)^2, \tag{1}$$

where p is the porosity of the ceramic and E is the elastic modulus. The elasticity of the buffer layer is proportional to the square of the volume fraction. So the more porous the buffer layer, the more the ceramic buffer layer will displace under a force and respond as an actual buffer.

No significant temperature gradient in the micro fuel particle is expected because these ceramics have reasonable thermal conductivities and small dimensions. Even if the buffer has a very conservative thermal conductivity of 2 W/m-K, because of a high porosity, only a 5 K temperature difference is expected for this small radius.

3. Results

Initially, the fuel particle will not have any internal stress when it is fabricated at 1600 °C, but stresses develop as it is cooled to room temperature. Thermomechanical stresses due to this cooling

Table 2
Material properties used in analyses

Material properties						
Materials	Elastic modulus (GPa)	Poisson's ratio	Thermal expansion	Creep		
				$\dot{\varepsilon} = A\sigma^n \exp\left(\frac{-Q}{RT}\right)$		
				A	n	Q (kJ/mol)
UN	265	0.27	Temperature	Not considered		
UC	225	0.28	dependent	Not considered		
TiC	470	0.19	see Fig. 2	229.3	3	500
SiC	410	0.14		3.01E-05	1	200
ZrC	400	0.19		6658767	3	600
TiN	465	0.25		N/A (TiC values used)		
ZrN	380	0.16		N/A (TiC values used)		
Buffer	Material and porosity dependent, see Eq. (1)	0.33	(Same as material)	(Same as material)		

period are provided below. Figs. 3 and 4 show the radial and tangential stresses, respectively, in the different candidate coatings, after cooling from fabrication. The cooling from fabrication causes the fuel to shrink more than any of the ceramic coatings, creating a tensile strain on the coatings in the radial direction and a compressive strain in the tangential direction for all material combinations analyzed. The stresses are dominated by tension in one direction and compression in the other (as can be seen in Figs. 3 and 4), because of the spherical design of the micro fuel particles. The large influence of the thermal expansion of different materials creates force in the radial direction (as will
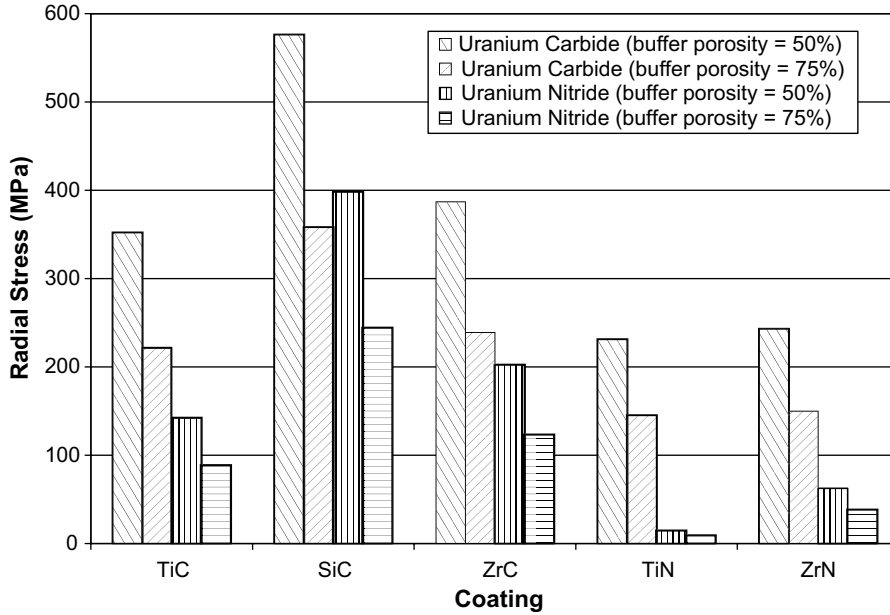
Fig. 3. Maximum radial stress in the coating material after cooling from 1600 °C to room temperature.
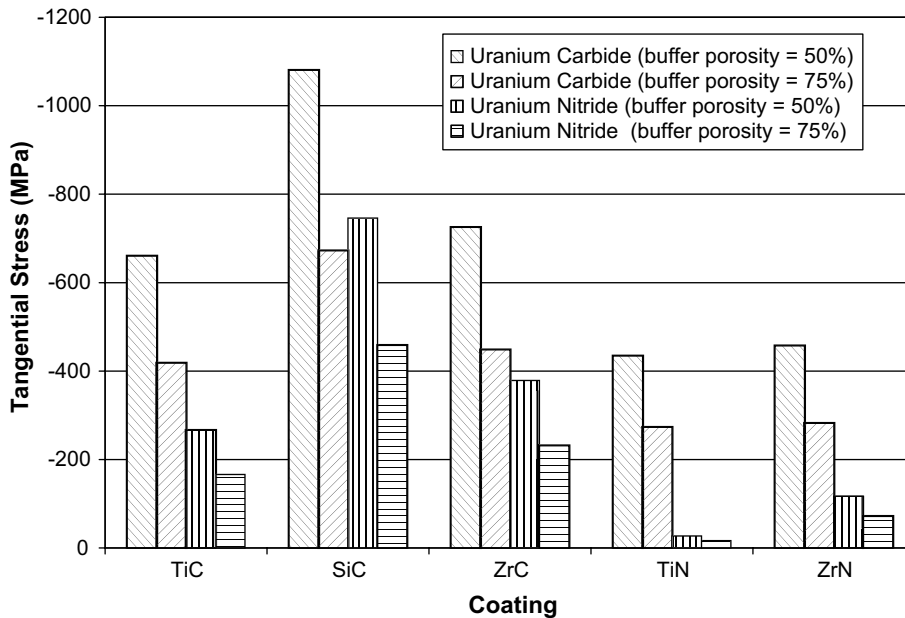

Fig. 4. Maximum tangential stress in the coating material after cooling from 1600 °C to room temperature.

all variables within the micro fuel particle system), and in turn this creates a reaction in the tangential direction.

By comparing Figs. 3 and 4, it can be seen that the absolute stress in the radial and tangential directions are similar to each other for different fuels, coatings, and buffer porosities. Because the radius of the coating stays fairly constant, the tangential stress divided by the radial stress will also remain at a fairly constant ratio of approximately two. Therefore one can infer the stress in the radial direction from the values given for the tangential stress in this study.

These different fuel and coating combinations and different buffer porosities vary in stress after cooling from fabrication because of two material properties: the thermal expansion and the elastic modulus. How well the elastic modulus can mitigate the stress can be seen by comparing the results for different buffer porosities. Typically, raising the buffer porosity from 50 to 75% and thus lowering its elastic modulus by a factor of 4 (according to Eq. (1)) will lower the stress in the coating by about 30%, as seen in Figs. 3 and 4. The relationship between the stress and the thermal expansion on the other hand, can be seen by comparing Fig. 2 with Figs. 3 and 4. If there was no difference in the CTE's of the coating and the fuels, the micro fuel particle would expand and shrink equally and there would be no stress. As can be seen in Fig. 2,

the CTE of the UN is much closer to all of the coatings than the UC. As a result, the UC creates more stress than the UN no matter what candidate coating is used. Also, it can be seen that the CTE for UN is very close to TiN. As expected, the stress in this coating is the lowest of all the fuel/coating combinations after cooling from fabrication.

The stresses in the 2nd period react in very much the same manner as they did in the 1st stress period. Once again, the dominant effect is the thermal expansion. In fact, by comparing Figs. 4 and 5, it can be seen that the different stresses in the 2nd period from the combinations of fuels and coatings have similar profiles, as compared to those from the 1st period, because the difference between the fuel and coating CTE at 20 °C and 1100 °C are similar, as can be seen in Fig. 1. Because the temperature difference from the fuel particle's equilibrium (1600 °C) is 500 °C in the 2nd stress period as opposed to the 1580 °C that it was in the 1st stress period, the magnitude of the stress drops proportionally. This can be seen by comparing the scales of the graphs of Figs. 4 and 5.

The 3rd stress period is unique, because in this period, reactor conditions must be considered. As said before, these conditions include fuel swelling, coating and buffer creep, and fission gas pressure buildup. To better understand the micro fuel particle model, all of these conditions were tested individually with UC/TiC.
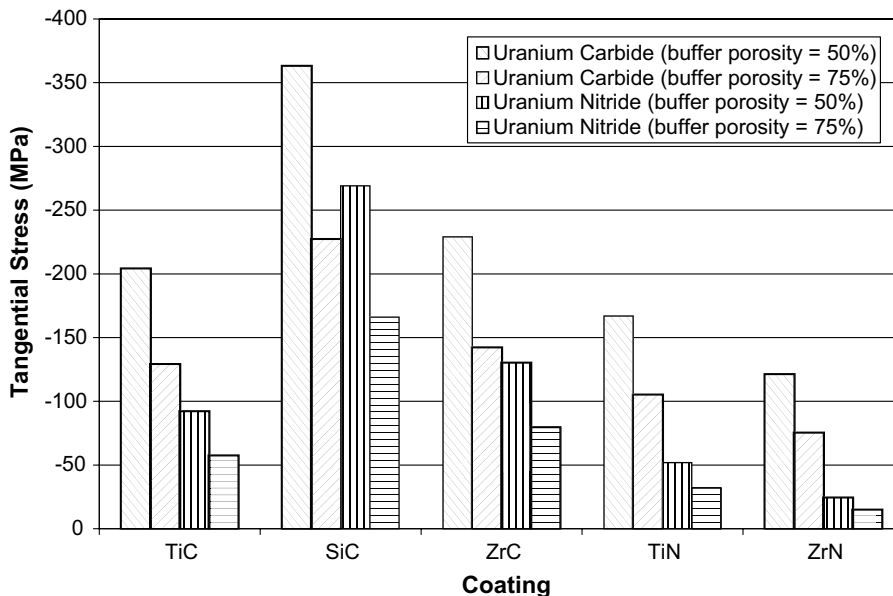

Fig. 5. Maximum tangential stress in the coating material at 1100 °C.

4. Fission gas pressure

One of the operational variables is the pressure from fission gas release. This pressure is modeled to increase over time as the gas is released from the kernel and accumulates in the porous buffer layer, which acts as a plenum. The fission gas pressure in the buffer was calculated to be 4.8 MPa per year in the first year, decreasing slightly to 4.69 MPa per year in the 3 year. These values used for the thermomechanical models are calculated from the Redlich–Kwong equation of state [7], with a conservative estimate of 95% fission gas release from both Xe and Kr. This pressure pushes against the outer coating, and produces stresses as shown in Fig. 6. As this figure shows, the gas pressure does not produce significant changes in the coating stress. The actual stresses are likely to be even lower than predicted by this model because the fission gas release fraction from UN fuel may be well below the assumed 95% at these temperatures [8].

This predicted stress change due to gas pressure of about 6 MPa is surprisingly small for this model, but after thorough analysis of several of the assumptions, it can be seen that this is accurate. Two of these assumptions are that this model has no debonding and a buffer porosity of 50%. If the buffer had a lower stiffness, it would not resist the pressure as much (or not at all if it debonded from the coating). When an analysis is done for the coating with 75% buffer porosity and the same pressure, the amount of stress change is 16 MPa. When a finite element analysis is carried out with no buffer or fuel kernel, but with the same pressure increase over 3 years, the coating is found to have a stress change of 26 MPa. This result can be roughly checked analytically with the formula for a thin shell pressure vessel:

$$\sigma_{\mathrm{p}}(3\ \mathrm{years}) = \frac{P \cdot r}{2t} \approx 14\ \mathrm{MPa} \cdot \frac{400\ \mu\mathrm{m}}{2 \cdot 100\ \mu\mathrm{m}} \approx 28\ \mathrm{MPa}.$$

Another assumption is the amount of applied pressure. The fission gas pressure release and the particle power of 63 mW are both functions of the assumed fuel fission rate density of 3×10^{13} fissions/cm^3-s. If it is decided that the particle power should be increased (thus increasing the fuel fission rate density), then the rate of pressure would also proportionally increase.

When comparing the new BISO fuel particle to the TRISO fuel particle, it is pertinent to take note of certain differences in the stress incurred from fission gas release. First of all, the BISO particle gas pressure is less than the TRISO because it is assumed that the BISO particle only releases Kr and Xe, and not CO or O$_2$ since there is no oxygen in the particle. Also, the TRISO fuel particle uses a different buffer material, so if its elasticity is lower than that of the new BISO fuel particle's ceramic buffer, the TRISO particle's buffer would not mitigate the stress as much as the BISO's buffer does. Finally, it is also important to recognize any differences in the particle power and the coating thickness.
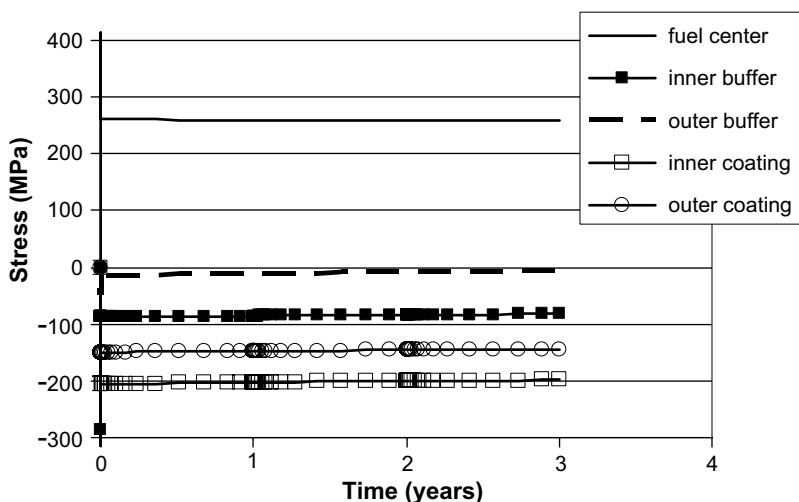

Fig. 6. Tangential stresses as a function of time, without creep or swelling. The change from startup, where there are no fission gases, to the end, indicate the additional stress caused by the gas pressure.

Another of the operational variables is fuel swelling. Swelling is one of the biggest concerns because of the type of fuels in consideration. Swelling in the fuel kernel for this analysis is considered to be isotropic and a function of the burn-up, temperature, and type of fuel.

The swelling for UC is expected to be dependent on temperature range, UC stoichiometry, and burn-ups. For this analysis, the temperature during operation is constant at 1100 °C, the fuel is assumed to always be stoichiometric, and the fuel fission rate density gives a burn-up of about 24,500 MWd/m per year. Matke shows that this would result in about 9% swelling per year in UC [9], and this is what is used for the swelling analyses. However, this may be an underestimate, because according to Ritzman [10], these parameters could lead UC to swell 14% a year. Fuel swelling data is even less extensive for UN, but nitrides tend to show less swelling than carbides [11]. UN appears to have a swelling rate half that of UC. Hence, a swelling rate of 4.5% per year is used for UN. The error associated with these numbers is expected to be large and have a number of different dependencies; however swelling for these materials is largely unknown and this will at the very least allow this study to gauge how important swelling is in the new BISO fuel particle.

Swelling was independently analyzed, once again using UC/TiC and a buffer porosity of 50%. Its effect can be seen in Fig. 7, which shows the dramatic increase in swelling stress with increasing burn-up (without creep relaxation). However, this analysis is simplified because it does not take into consideration that the elastic modulus in the fuel is dependent upon swelling and temperature. According to Cahn [12], a temperature of 1100 °C will lower the elastic modulus by 10% in both UC and UN. He also reports the dependence of the elastic modulus of UC and UN as functions of fuel porosity. Increased porosity in the form of vacancies and gas bubbles is the major cause of swelling for these fuels. Assuming a swelling rate of 9% per year for UC, the fuel will have 27% porosity after 3 years. As reported by Cahn [13], the dependence of UC on porosity is:

$$E_p = 224.9(1 - 2.30 \times p). \tag{2}$$

Therefore the elastic modulus of UC will decrease by 49% after swelling for 3 years. These two changes in the elastic modulus will decrease the maximum tangential stress in the coating in Fig. 9 to 8.0 GPa.

It is also important to recognize that swelling rate, as stated before, is dependent on the burn-up rate. However, the burn-up rate depends on particle power, which is rated at 63 mW for these results. If it is decided that more power is desired, this would proportionally increase the swelling rate as it would the gas pressure rate. This study recognizes at least 5 known possibilities which may help mitigate the stress from swelling: buffer porosity, fuel selection, coating swelling, particle parameters, and coating creep.
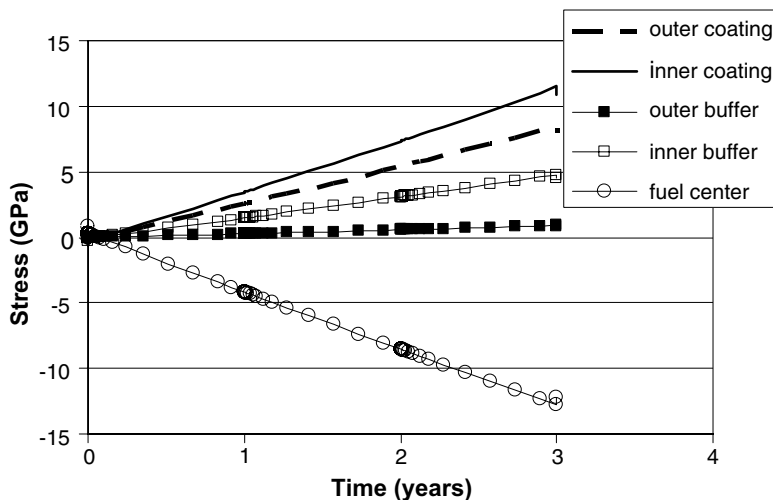

Fig. 7. Tangential stress in the coating from the fuel swelling over the 3 years. No creep is included in this analysis, to demonstrate the potential of swelling to produce large stresses.

The first two possibilities which could help mitigate this stress are increasing the buffer porosity and using a different choice of fuel. Both of these were analytically tested, and can be seen below in Figs. 8 and 9. It can be seen that increasing the porosity from 50 to 75% is expected to decrease the stress from swelling by about a third when swelling is the only inelastic strain considered. The analysis shows that the use of UN instead of UC cuts the amount of stress on the coating in half because it swells half as much. However, that analysis is again done without regard to the fact that the elastic modulus is dependent on porosity. The elastic modulus for UN is [13]:

$$E_p = 260.4(1 - p)^{3.002}. \tag{3}$$

The elastic modulus for UN is only expected to drop 32% from swelling over 3 years, because the swelling rate is not as great. Therefore, the true maximum stress in the coating from just swelling of UN is 4.8 GPa. Therefore, the use of UN instead of UC reduces the tangential coating stress by 40% in this benchmark.

Another possibility to reduce the stress in the coating is the coating swelling itself. Just as in the case of the thermal expansions, if the fuel and the coating expand at the same rate, there will be no applied pressure between the layers. Swelling
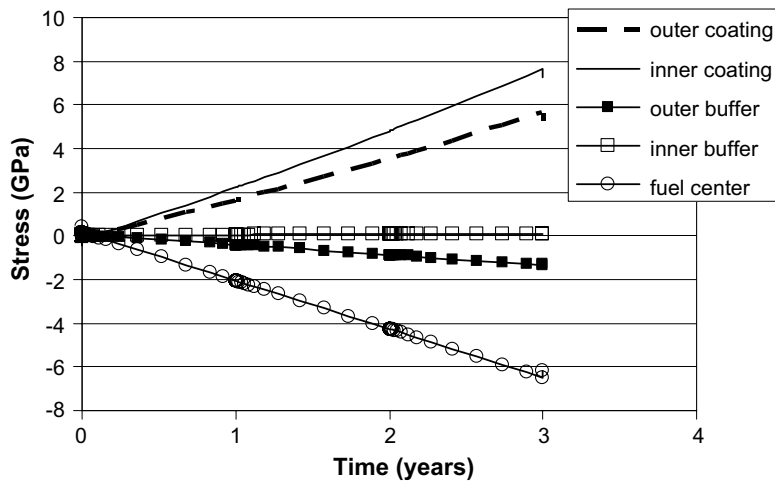

Fig. 8. Tangential stress from swelling over the 3 years in the BISO fuel particle with an increased buffer porosity of 75%.
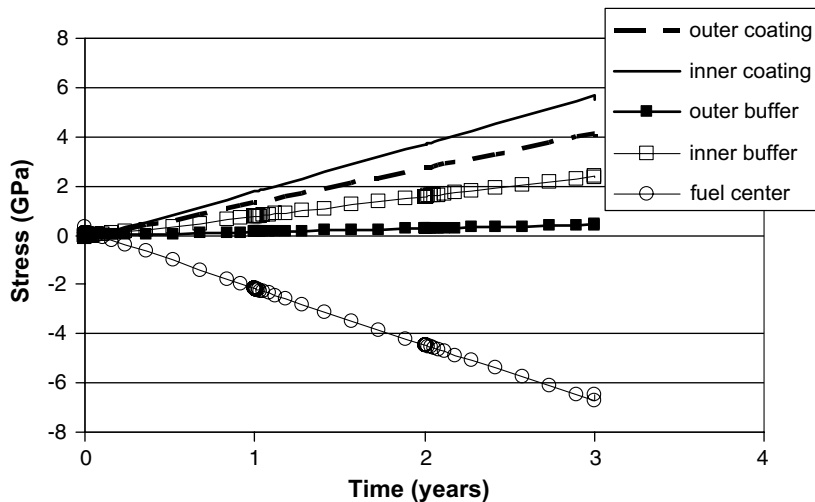

Fig. 9. Tangential stress from swelling over the 3 years in the BISO fuel particle with UN as the fuel.

for these types of materials is largely unknown. However, contrary to previous studies, SiC has shown significant void swelling up to ~5% starting at 1000 °C [5]. Coating swelling would reduce stress between the fuel and the coating; however low coating swelling is also a requirement given for the GFR fuel matrix materials [14].

The last two possibilities to help mitigate the coating stress are changing the dimensions of the micro fuel particle and coating creep. Intuitively, increasing the thickness of the buffer layer will allow the fuel to swell more, and/or increasing the thickness of the coating will give the coating more structural integrity.

5. Creep

The last variable during reactor operation is creep. Thermal creep follows the relationship given in the equation:

$$\dot{\varepsilon} = A\sigma^n \exp\left(\frac{-Q}{RT}\right), \tag{4}$$

where $\dot{\varepsilon}$ is the strain rate, σ is the applied stress (in a uniaxial test), Q is the free energy of the material, T is 1100 °C, and A and n are material dependent constants given in Table 2. As can be seen in this table, creep data for the nitride coatings is not available, so a proper analysis cannot be done for these materials. Instead, TiC creep data is used for the nitrides, so a rough analysis can be done. The amount of

creep from irradiation is also unknown, but could have large effects on the fuel particle system. Creep is considered in both the buffer and in the coating, but it is unnecessary to consider it in the fuel, because the fuel is hydrostatic. Creep is independently analyzed under the same benchmark with a UC/TiC combination and 50% buffer porosity, just as fuel swelling and fission gas pressure release are. This effect of creep can be seen in the Fig. 10. It can be seen that the thermal creep will relax the stress incurred from the thermal expansion on time scales of the order of months and the thermal stress will converge towards zero. The creep will allow the coating to deform and the pressure between the layers of the micro fuel particle to come to equilibrium. The same is true for 75% buffer porosity, as can be seen in Fig. 11.

6. Full power operation

When all of the operational variables are used in conjunction with each other as we would expect during the reactor operation, it can be seen that the variables have an effect on each other, as seen in Fig. 12. Simply put, the stresses incurred from the individual operational variables do not simply 'add'. In the previous sections, we saw that fission gas pressure was relatively insignificant, swelling created run-away stress, and creep would allow for slow relaxation until there was no more stress in the coating. Now it can be seen that there is a
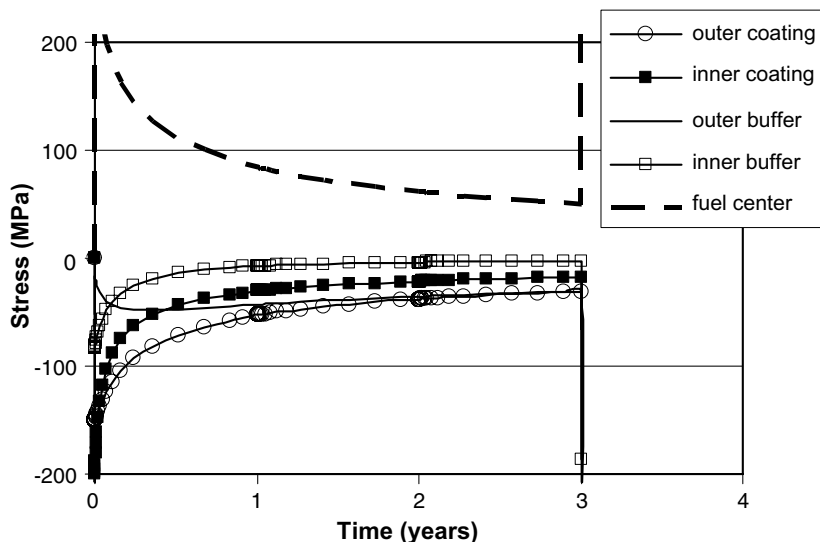
Fig. 10. The influence of thermal creep on tangential stress for 3 years in the BISO fuel particle (without swelling).
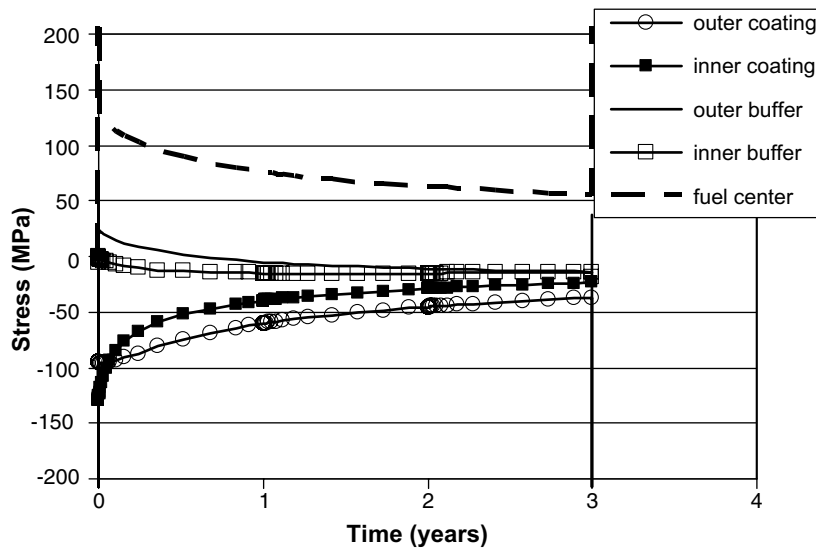
Fig. 11. The influence of thermal creep on tangential stress for 3 years in the BISO fuel particle with an increased buffer porosity of 75% (without swelling).
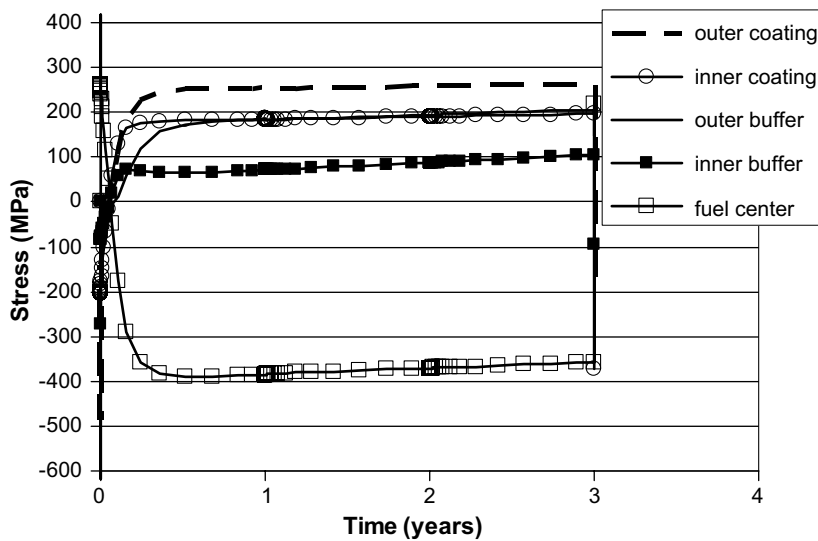

Fig. 12. Tangential stress in the BISO fuel particle during 3 years of reactor operation.

steady-state stress, reached when the initial thermal stresses have relaxed away and the swelling and creep strains balance each other. All of the fuel/coating combinations were analyzed, and the steady-state stress values (which are also the maximum) are reported in Fig. 13. It is significant to note that the tangential stress is tensile, as opposed to the results from the 1st and 2nd stress periods.

UC creates higher levels of stress than UN, because of the higher swelling rate. Among the coat-

ings, SiC has the greatest amount of stress, because it has the lowest creep rate at this temperature and these stresses. Also, the swelling and creep rates overwhelm all other considerations, because the coatings with no creep data (in which TiC data was used) have the same stress values as TiC. The dichotomy of swelling and creep diminish the importance of all other factors. As seen in Fig. 13, even the buffer porosity has an insignificant effect on the steady-state stress.
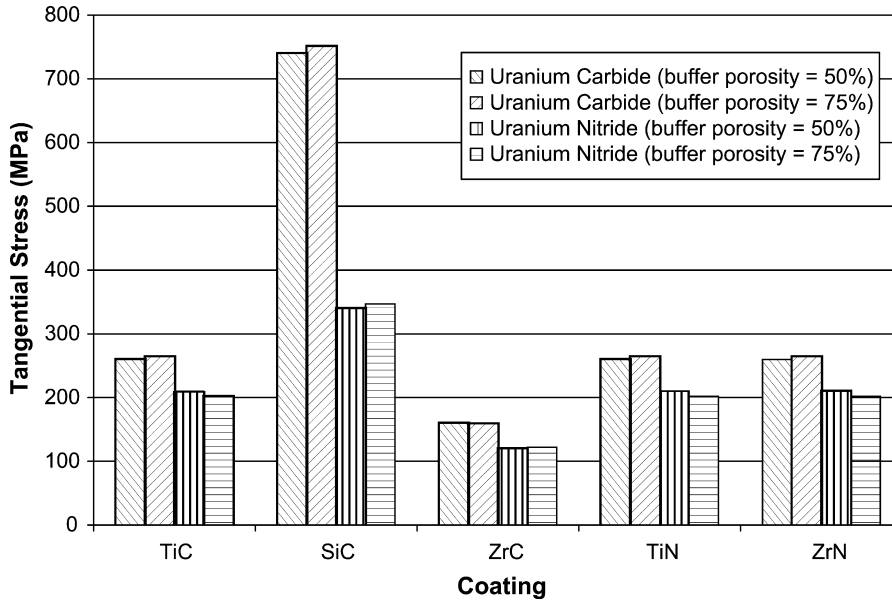
Fig. 13. Maximum tangential stress in the coating materials during reactor operation.

7. Shutdown

After the micro fuel particles have operated for a fuel cycle, they will be brought back down to room temperature. Therefore, the differential thermal expansion in the micro fuel particle will once again change the stress in the coating. The maximum stress for the different fuel/coating combinations

for this 4th stress period can be seen in Fig. 14. This figure may be confusing at first compared to the other stress periods, because depending on the fuel and coating combination, some tangential stresses will return to compression while others will remain in tension. This however, becomes clear if one realizes that the stress in the coatings at room temperature would be exactly the same as they were before
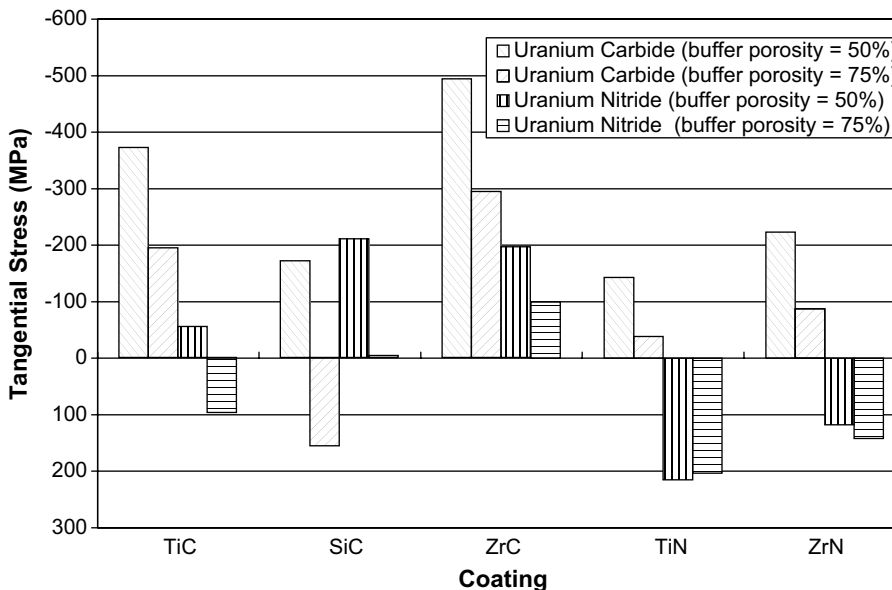

Fig. 14. Maximum tangential stress in the coating materials after reactor operation.

the reactor operation if there was no swelling, creep, and fission gas release. In fact, the tangential stress increase from 20 °C (1st stress period) to 1100 °C (2nd stress period) is identical to the decrease from the end of reactor operation (3rd stress period) to room temperature (4th stress period). This can be seen by comparing the stress difference of Figs. 13 and 14 with the difference between Figs. 4 and 5.

8. Fracture model

A likely failure mode of coated-fuel particles is fracture of the coating, leading to release of fission products. Such fracture is likely to be caused by tensile stresses such as the ones discussed in the previous sections. To address these issues, fracture mechanics models have been employed to study the effects of flaws within the coating.

The most critical flaw in a spherical shell coating will typically be an elliptical flaw either embedded within the coating or at the inner coating surface. No model is available for elliptical flaws in spherical shells, but simplified models are adequate for the current application.

There are existing fracture models for through-cracks in spherical shells [15,16] and, in comparing the results to those for through cracks in flat plates, one finds that sufficiently thin spherical shells behave identically to flat plates. This is shown in Fig. 15, which shows the stress intensity as a function of crack size for both a thin spherical shell and a flat plate. As can be seen, for width or circumference of 880 μm and a thickness of 40 μm, the results are identical for crack sizes below about 20 μm. Hence, for small cracks, a flat plate model should be adequate for the preliminary assessment of the coatings considered in this paper.

These results have been obtained using the following equations. The stress intensity K_I caused by a finite line crack of width $2a$ in a thin plate of width W and thickness t is given by:

$$K_I = \sigma \cdot (\pi \cdot a)^{\frac{1}{2}} \cdot \left[\frac{W}{\pi \cdot a} \cdot \tan\left(\frac{\pi \cdot a}{W}\right) \right]^{\frac{1}{2}}. \qquad (5)$$

In a thin spherical shell of radius R and thickness t a finite line crack of the size $2a$ leads to a stress intensity of [17]:

$$K_I = \sigma \cdot (\pi \cdot a)^{\frac{1}{2}} \cdot (1 + 1.41\lambda^2 + 0.04\lambda^3)^{\frac{1}{2}}$$
$$\text{with } \lambda = \frac{a}{(R \cdot t)^{\frac{1}{2}}}. \qquad (6)$$

Fracture models for elliptical cracks in flat plates are readily available. For such a crack with major radius b and minor radius a, the maximum stress intensity is given by:

$$K_I = \sigma \cdot (\pi \cdot a)^{\frac{1}{2}} \cdot \frac{1}{E(k)}, \qquad (7)$$
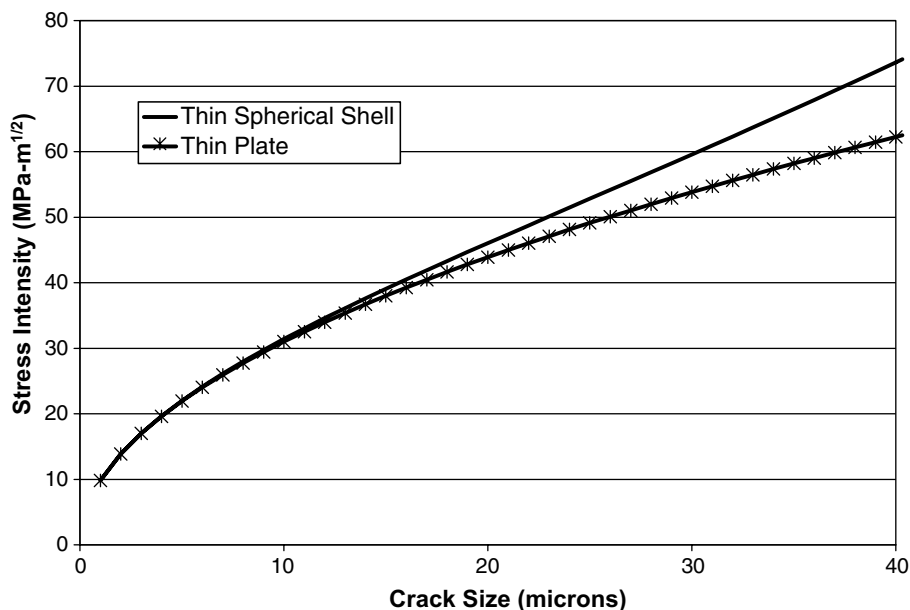

Fig. 15. Stress intensity factor for a thin plate and a spherical shell. Thicknesses are 40 μm; circumference and plate width are 880 μm.

where

$$E = \int_0^{2\pi} (1 - k^2 \cdot \sin^2 \varphi)^{\frac{1}{2}} \mathrm{d}\varphi \quad \text{with } k = \left(1 - \frac{a^2}{b^2}\right)^{\frac{1}{2}}.$$

(8)

This elliptical crack is assumed to be embedded within the coating. A modified version is the semi-elliptical surface crack, where the crack is located directly on the surface:

$$K_{\mathrm{I}} = \sigma \cdot (\pi \cdot a)^{\frac{1}{2}} \cdot \frac{G}{E(k)} \quad \text{with } G = 1.12.$$

(9)

The results for the stress intensity factor from these two geometries is shown in Fig. 16 for the case of $b = 2a$. It is clear from this figure, that for the same crack size the surface cracks are more likely to grow. Hence, only these cracks will be considered further.

In determining the failure loads for these coatings, one must compare the calculated stress intensity factor for a given load and geometry to the fracture toughness of the coating material. For polycrystalline silicon carbide (SiC), the fracture toughness is in the range $2.8 \, \mathrm{MPa}\sqrt{m} \leqslant K_{\mathrm{I,c}}^{\mathrm{SiC}} \leqslant 3.4 \, \mathrm{MPa}\sqrt{m}$ [20], but it exhibits a strong dependence on temperature and material processing. For single-crystal SiC one finds $K_{\mathrm{I,c}}^{\mathrm{SiC}} = 3.3 \, \mathrm{MPa}\sqrt{m}$ for temperatures below 500 °C, but approaching a value of $5.8 \, \mathrm{MPa}\sqrt{m}$ at 1500 °C [18]. For sintered SiC slightly elevated values ($3.8 \, \mathrm{MPa}\sqrt{m} \leqslant K_{\mathrm{I,c}}^{\mathrm{SiC}} \leqslant 5.6 \, \mathrm{MPa}\sqrt{m}$, increasing with sintering temperature) are reported [19]. For hot pressed SiC the range $2.9 \, \mathrm{MPa}\sqrt{m} \leqslant K_{\mathrm{I,c}}^{\mathrm{SiC}} \leqslant 4.5 \, \mathrm{MPa}\sqrt{m}$ is reported [20]. It should be noted that the hot pressed and sintered forms of SiC differ markedly in their temperature dependence. While $K_{\mathrm{I,c}}^{\mathrm{SiC}} = 3.1 \, \mathrm{MPa}\sqrt{m}$ for sintered SiC, with a gradual increase with temperature above 1200 °C, the fracture toughness of the hot pressed version ($K_{\mathrm{I,c}}^{\mathrm{SiC}} = 3.7 \, \mathrm{MPa}\sqrt{m}$) dramatically decreases with temperature above 1100 °C (to $K_{\mathrm{I,c}}^{\mathrm{SiC}} \leqslant 2.6 \, \mathrm{MPa}\sqrt{m}$ at 1400 °C).

For titanium carbide (TiC), the amount of available data is small, but it seems to exhibit a consistently higher toughness than SiC. A value of $K_{\mathrm{I,c}}^{\mathrm{TiC}} = 7.8 \, \mathrm{MPa}\sqrt{m}$ is reported [21,22] for room temperature. For single-crystal TiC a range of far lower values, $1.50 \, \mathrm{MPa}\sqrt{m} \leqslant K_{\mathrm{I,c}}^{\mathrm{TiC}} \leqslant 3.58 \, \mathrm{MPa}\sqrt{m}$ is reported [23], where the actual value is strongly dependent on direction. A lower range is given for hot pressed TiC ($3.53 \, \mathrm{MPa}\sqrt{m} \leqslant K_{\mathrm{I,c}}^{\mathrm{TiC}} \leqslant 4.59 \, \mathrm{MPa}\sqrt{m}$) [24]. Although ZrC, TiN, and ZrN is not considered, future work is planned to look more in depth at these materials and their resistance to crack propagation.

Using the results for stress intensity factors for surface elliptical flaws in flat plates, one can compare the allowable pressures for fixed geometries and varying materials. The results are shown in
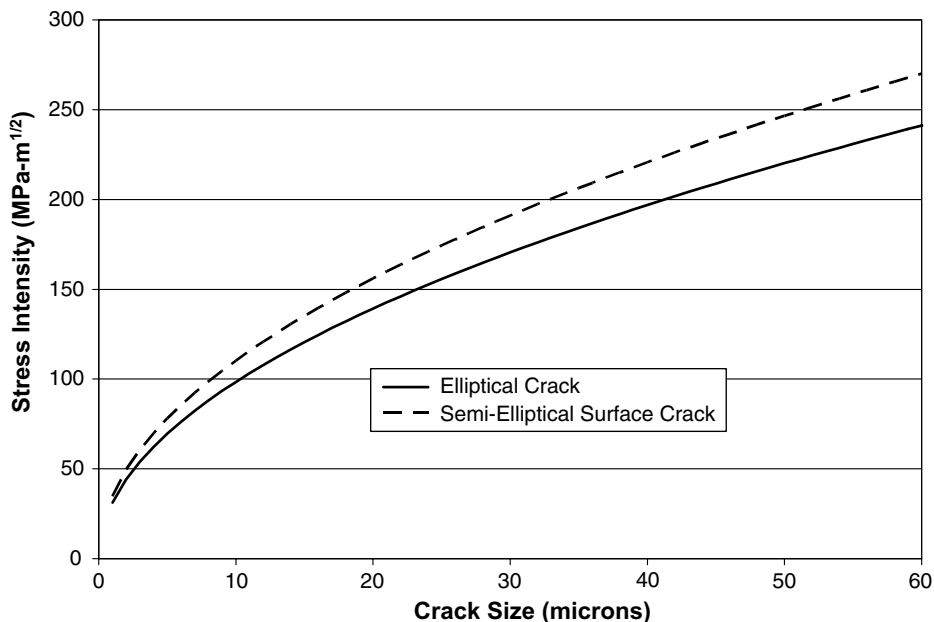

Fig. 16. Stress intensities vs. crack size for embedded and surface elliptical cracks for $b = 2a$.
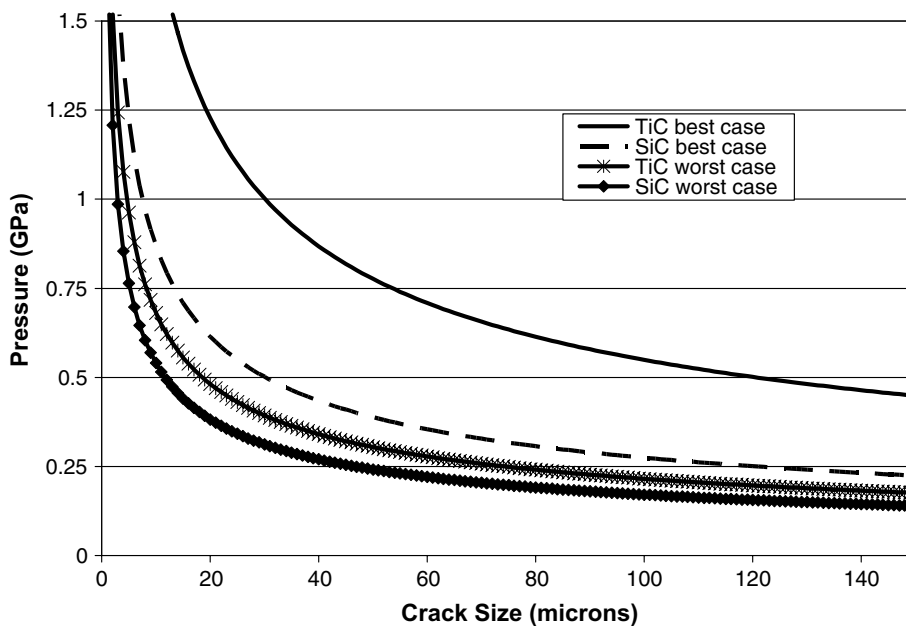
Fig. 17. Allowable pressure for an elliptical surface flaw in a spherical shell for various materials.

Fig. 17, which shows that the TiC coatings are more fracture resistant than SiC.

9. Conclusions

Finite element models have been used to compare the thermomechanical performance of a series of candidate fuels and coatings for BISO fuels applicable to high temperature gas reactors. In the 1st, 2nd, and 4th stress periods when there is no swelling or appreciable creep, the key parameters are differential thermal expansion and buffer porosity. During operation, the primary influences are creep and swelling.

When interpreting the results of the coating stress in each stress period in Figs. 4, 5, 13 and 14 to determine which materials are best, it is important to remember that ceramics can typically tolerate compressive stresses approximately eight times the fracture stress in tension, according to the Griffith criterion [25]. Therefore, by comparison of the stresses during the different periods, this research predicts that for almost any combination of fuel and coatings, tangential tensile stress during reactor operation creates the most likely failure point. Of the different fuel and coating combinations, UN/ZrC has the lowest tensile stress at this point. It could then be said that UN/ZrC is the best selection if all the coatings had the same failure stress, and

UN/TiN and UN/ZrN could also be strong candidates if their creep rates were sufficiently large. However, these ceramics do not have the same resistance to crack propagation, as TiC's resistance to cracking is greater than SiC as seen in the fracture analysis above. A more thorough fracture analysis would have to be done in order to determine which ceramics best resist crack propagations for these given stresses.

Also, these figures only show the stress in the tangential direction, but there is also stress in the radial direction, which is typically half the magnitude of the tangential stress and of opposite sign. A failure in the ceramic resulting from radial stresses would likely produce azimuthal flaws, so it would not necessarily produce a release path for fission gases. However, it could create tangential stress concentrations and subsequent compromise of the BISO coating.

Acknowledgement

References

[1] M.K. Meyer, N. Chauvin, Overview of gas fast reactor inert matrix fuel candidates. Global 2003, New Orleans, LA, November 16–20, 2003.

[2] Y.S. Touloukian et al., Thermophysical properties of matter: thermal expansion nonmetallic solidsPurdue Research Foundation, vol. 13, IFI/Plenum, NY-Washington, 1977.

[3] R.W. Cahn et al., Materials Science and Technology: Nuclear Materials. V. 10A, Table 4–20, Line 2.

[4] R.W. Cahn et al., Materials Science and Technology: Nuclear Materials. V. 10A, Table 4–20, Line 11.

[5] S.J. Zinkle, N.M. Ghoniem, Fus. Eng. Des. 51–52 (2000) 55.

[6] A. Sherman et al., Refractory ceramic foams: A Novel New High Temperature Structure. Ultramet, Pacoima, CA. http://www.ultramet.com/foamtech.htm.

[7] Development of improved models and designs for coated-particle gas reactor fuels. Final Report Under the International Nuclear Energy Research Initiative (I-NERI). December, 2004, p. 20.

[8] M. El-Genk, A critical review of space nuclear power and propulsion 1984–1993, American Institute of Physics, New York, p. 201, Fig. 18(b).

[9] Hj. Matzke, Science of Advanced LMFBR Fuels, North-Holland, 1986, p. 463, Fig. 9.2.

[10] R.L. Ritzman et al., Nucl. Appl. Technol. 9 (2) (1970) 167, Fig. 21.

[11] Hj. Matzke, Science of Advanced LMFBR Fuels, North-Holland, 1986, p. 531.

[12] R.W. Cahn, et al., Materials Science and Technology: Nuclear Materials. V. 10A, Table 4–22.

[13] R.W. Cahn, et al., Materials Science and Technology: Nuclear Materials. V. 10A, Table 4–21.

[14] M.K. Meyer, N. Chauvin, Overview of gas fast reactor inert matrix fuel candidates, Global 2003, New Orleans, LA, November 16–20, 2003.

[15] E.S. Folias, Int. J. Fract. Mech. 1 (1965) 20.

[16] F. Erdogan, J.J. Kibler, Int. J. Fract. Mech. 5 (1969) 229.

[17] F. Erdogan et al., Int. J. Fract. Mech. (1969) 229.

[18] J.J. Bellante, H. Kahn, Appl. Phys. Lett. 86 (2005) 071920.

[19] J.L. Henshall et al., J. Am. Ceram. Soc. 60 (1977) 373, Discussions and notes.

[20] Y.-W. Kim et al., J. Mater. Sci. 35 (2000) 5569.

[21] T.T. Shih, J. Opoku, Eng. Fract. Mech. 12 (1979) 479.

[22] G.S. Upadhyaya, Nature and Properties of Refractory Carbides, Nova Science Publishers, 1996.

[23] J.L. Chermant et al.Fracture Mechanics of Ceramics, vol. 4, Plenum Publishing, 1978, p. 891.

[24] C. Maerky et al., Mater. Sci. Eng. A 209 (1996) 329.

[25] M.A. Meyers, K.K. Chawla, Mechanical Behavior of Solids, Prentice Hall, Upper Saddle River, N.J, 1999, p. 155.

Further reading

[1] C.A. Daniels, Ceramics: Structure and Properties, Mechanical Properties, Abyss Books, Washington D.C., 2002, p. 123.